Hindawi
International Journal of Aerospace Engineering
Volume 2024, Article ID 8841710, 12 pages
https://doi.org/10.1155/2024/8841710

Research Article

Investigation and Validation of Mission Evaluation Models for Space Close-Range Inspection

Jianyong Zhou,[1,2] Zhipu Hou,[3] and Kebo Li[1,2]

[1]*College of Aerospace Science and Engineering, National University of Defense Technology, Changsha 410073, China*
[2]*Hunan Key Laboratory of Intelligent Planning and Simulation for Aerospace Mission, Changsha 410073, China*
[3]*Northwest Institute of Nuclear Technology, Xi'an 710024, China*

Correspondence should be addressed to Kebo Li; likeboreal@nudt.edu.cn

Received 21 August 2023; Revised 5 December 2023; Accepted 29 December 2023; Published 24 January 2024

Academic Editor: Fangzhou Fu

Space close-range inspection can be used to carry out close-range observation and monitoring of targets for identifying the target's types and working states, which is of great significance for space missions such as in-orbit services. The effectiveness evaluation of space inspection tasks will significantly affect the studies on the trajectory design, orbit motion control, and task termination conditions. However, the evaluation models in previous studies are too simple such as that they are usually without considering dynamic changes in the satellite orbit relative motion. Besides, these studies fail to build a comprehensive evaluation model for the whole inspection task process. In this paper, taking the most commonly used optical inspection as an example, the novel multifactor inspection task effectiveness evaluation models were investigated, including the constraint models of observation, the relative distance evaluation model, the effective observation time evaluation model, and the target observation angle evaluation model. These models solve the effectiveness evaluation problem for the complete process of an inspection task, which can support the design of inspection strategies and trajectories better by using the evaluation results. In addition, numerical simulations and 20 semiphysical experiments were carried out to validate the proposed evaluation models.

1. Introduction

Along with the development of space technologies, the demand for close-range control for orbit services and space countermeasures, such as target capture and fault repair, increases strongly. For verifying the type of target, identifying the target's status or locating the target's faults, etc., the optical inspection for space targets is mostly used. Efficiency evaluation can quantitatively evaluate the completion and efficiency of inspection tasks, support the optimization design of inspection tasks, and enhance the mission capability of inspection spacecraft.

Currently, there are many studies on the observation conditions, sensor hardware optimizations, and evaluations of observation images for close-range optical observation. Weiss et al. developed a performance evaluation model for the evaluation of space station inspection task, which is consisted of the percentage of anomalies detected and the time taken to complete the inspection [1]. Boskovic et al. developed an integrated mission planning and autonomous control technology system including the closed-loop sensor response, online learning about the environment, and reactive mission planning. This system has been used in NASA Langley's research project ISR (Intelligence Surveillance Reconnaissance) [2]. Meister et al. introduced some methods for modeling and assessing an imaging sensor that could be used in the aerospace industry for camera-based inspection [3]. Neta and Vallado gave a solution in the case of a cylindrical shadow for calculating the elliptical orbits' earth shadow speedily in the inspection [4]. Sheikh et al. gave out the quality assessment algorithms that could be used to automatically assess the quality of images or videos in a perceptually consistent manner [5]. Yang et al. analyzed spatial object visibility models such as earth shadow constraints and solar interference constraints [6]. Wang et al. conducted a simulation analysis on the close-range inspection imaging process of the GSSAP (Geosynchronous Space Situational Awareness Program) satellite and found that when observing high-earth-orbit (HEO)

targets, it is necessary to comprehensively consider the observation distance, sunlight, and observation angle to obtain good imaging results [7]. Zhao et al. simulated and analyzed the space debris detection capabilities of space-based optical observation systems in low-earth orbit and subsynchronous transfer orbit [8]. Wang et al. used an image motion measurement method based on remote sensing images to study the problem of obtaining high-quality observation images by obtaining the displacement between adjacent frames through registration algorithms [9]. Ying et al. analyzed the factors that affect the detection distance and established a mathematical model for the maximum detection distance of the optical observation system [10]. Lin-ling investigated the quality evaluation of remote sensing images related to subjective vision and proposed a method of the clarity quality [11]. Lu analyzed the characterization parameters of remote sensing image quality and obtained a comprehensive characterization and evaluation method through principal component analysis [12].

These studies can improve the ability of inspection spacecraft for obtaining high-quality images with discreting states of the target. However, there are still some issues that need further research:

(1) The above-mentioned models usually consider relatively single evaluation element. Almost all of them just focus on the imaging quality evaluation under different lighting conditions or different relative distances. They have not considered the dynamic changes in the relative motion of satellite orbits

(2) The above studies mainly focus on the static evaluation of some discrete points during the inspection process, but they have not established any model to evaluate the achievement and efficiency for the entire observation task. For example, several high-quality discrete observations of the target at a fixed position may be valueless comparing with a 30 minutes continuous and multiangle observation

(3) The validation of models or algorithms in the previous literatures mainly involves theoretical simulations or some single-device experiments such as the experiments based on cameras only. These simulations or experiments cannot validate the various elements in the inspection process comprehensively

The main reasons may be that the inspection task involves multiple factors, such as lighting constraints, variabilities of position, and speed during the inspection as the same as the variabilities of different inspection task trajectories. Thus, it is complex to construct a comprehensive evaluation model. In addition, space inspection motions include the relative orbital motions and the respective attitude motions of two satellites. The simulation of motions should be more than 9 degrees of freedom, making it difficult to conduct physical ground validation experiments.

On the contrary, this paper focuses on the evaluation of the whole inspection process and provides a new effective evaluation method for the comprehensive evaluation of space close-range inspection tasks. It is organized as follows: In Section 2, the typical constraint models were introduced, including sunlight constraint and camera performance constraint. In Section 3, based on the factors such as relative distance, image movement, effective observation time, and target observation angle, the quantitative evaluation model for the comprehensive effectiveness of the whole inspection task is derived. After that, numerical simulations and 20 times semiphysical comprehensive experiments with 2 different conditions were carried out and analyzed, respectively, in Section 4 and Section 5.

2. Space Inspection Constraint Models

2.1. Problem Identification. Considering mass and size limitations, the inspection spacecraft usually need to approach their targets within about 10 km to conduct effective optical observations and obtain clear images. According to the data from the ISON (International Scientific Optical Network) space monitoring network of the Russian Academy of Sciences, GSSAP satellites conducted 9 close-inspection missions from 2016 to 2020, and all these inspections were realized within a relative distance of 10-15 km [13].

Therefore, the evaluation of inspection effectiveness in this paper is defined as the effectiveness evaluation of the inspection process which means the inspection spacecraft within a distance of about 10 km from the target. The other tasks, i.e., the long-range approach process of the target, are not included in this evaluation scope.

2.2. Constraint Models. Based on the problem's definition above, the close-range optical inspection observation mainly considers ground shadow constraint, sunlight angle constraint, and relative angular velocity constraint. When the ground shadow constraint is modeled, the inspection spacecraft can be approximately seen as overlapping with the position of the target spacecraft.

2.2.1. Ground Shadow Constraint Model. Assuming that the geocentric vector of the target spacecraft is r_e, the geocentric vector of the sun is r_s, and the angle between r_e and r_s is α, then, the target spacecraft can be observed when

$$0 \le |\alpha| \le \frac{\pi}{2}. \tag{1}$$

2.2.2. Sunlight Angle Constraint Model. Space-based optical observation needs to ensure that sunlight does not directly enter the camera's field of view; that is, the sum of the apparent radius of the sun and its light scattering angle is not within the camera's field of view, as shown in Figure 1.

θ is the field of view angle of the inspection spacecraft camera, β is the angle between the relative position vector of the target spacecraft and the relative position vector of the sun, θ_0 is the sum of the apparent radius of the sun and its light scattering angle, $0 < \theta_0 < \pi/2$, $0 \le |\beta| \le \pi$, and then, the sunlight angle constraint is

$$\frac{\theta}{2} + \theta_0 < \beta. \tag{2}$$

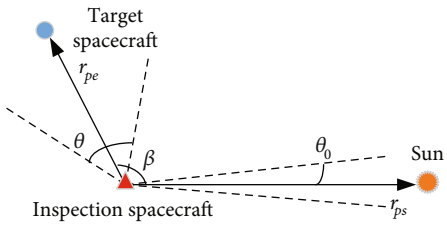

Figure 1: Schematic diagram of sunlight angle constraint.

It can be represented as a vector

$$\frac{\theta}{2} + \theta_0 < \arccos \frac{r_{pe} \times r_{ps}}{|r_{pe}||r_{ps}|}. \tag{3}$$

2.2.3. Observation Angular Velocity Constraint Model. Due to the performance of optical sensors, the angular velocity of sight line between the inspection spacecraft to the target cannot be too large; otherwise, the sensor may not be able to capture the target because of insufficient integration time of the camera imaging unit.

The maximum angular velocity which can be recognized by the inspection spacecraft sensor is $\omega_{\max}$, the relative velocity of the target to the inspection spacecraft is v_r, the angle between the relative velocity vector and the target's relative position vector r_{pe} is γ, and the observed angular velocity is ω, as shown in Figure 2.

Derived from velocity relationship

$$v_r \sin \gamma = \omega |r_{pe}|. \tag{4}$$

According to the relationship between v_r and r_{pe},

$$\gamma = \arccos \frac{r_{pe} \cdot v_r}{|r_{pe}||v_r|}. \tag{5}$$

From equations (4) and (5), it can be derived that

$$\omega = \frac{v_r}{|r_{pe}|} \sin \left(\arccos \frac{r_{pe} \cdot v_r}{|r_{pe}||v_r|} \right). \tag{6}$$

The observed angular velocity constraint is

$$\frac{v_r}{|r_{pe}|} \sin \left(\arccos \frac{r_{pe} \cdot v_r}{|r_{pe}||v_r|} \right) \le \omega_{\max}. \tag{7}$$

$\omega_{\max}$ is related to the exposure time and pixel size of the observation camera and is mainly determined by the hardware of the observation camera.

3. Space Inspection Effectiveness Evaluation Models

3.1. Relative Distance Evaluation Model. The size of the target spacecraft in the observation images directly affects the optical observation effect, while the imaging size is mainly

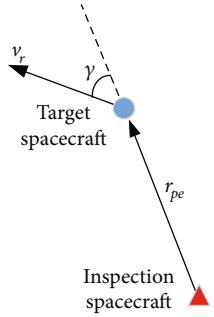

Figure 2: Schematic diagram of relative angular velocity constraint.

determined by the performance of the observation sensor and the relative distance of the target spacecraft. Note that f is the focal length of the inspection camera, H is the relative distance of the target spacecraft, and d and b are the height and width of the CCD camera target surface, as shown in Figure 3.

When the distance between the lens and the target spacecraft is H, the maximum width B and maximum height D that the camera can measure are

$$\begin{aligned} D &= \frac{dH}{f}, \\ B &= \frac{bH}{f}. \end{aligned} \tag{8}$$

The actual length corresponding to the unit image length is μ

$$\mu = \frac{D}{d} = \frac{B}{b} = \frac{H}{f}. \tag{9}$$

The actual width β_b and length β_d corresponding to each pixel are

$$\begin{aligned} \beta_b &= k_b \mu = k_b \frac{H}{f}, \\ \beta_d &= k_d \mu = k_d \frac{H}{f}, \end{aligned} \tag{10}$$

where $k_b \times k_d$ is the pixel size.

Therefore, the closer the distance, the larger the imaging of the target. However, if the distance is too close, a complete image of the target cannot be obtained which means that the observation requirements are not well filled. The observation effect is best when the target spacecraft is fulfilled with the entire pixel. To simplify the discussion, assuming that the target is a $L \times L \times L$ cube satellite and the image plane of the inspection camera is square, i.e., $b = d = l$, when the target spacecraft is fulfilled with the entire pixel

$$\frac{L}{H} = \frac{l}{f}, \quad i.e., H = \frac{Lf}{l}. \tag{11}$$

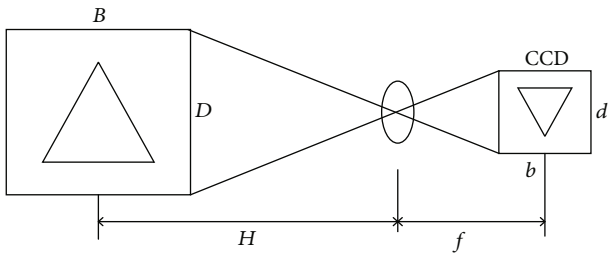

Figure 3: Schematic diagram of CCD camera imaging.

Therefore, the observation effect is best at a relative distance $H = Lf/l$.

When $H < Lf/l$, a valid and complete photo cannot be obtained, and the observation efficiency of the observation point will be scored as zero. When the relative distance is too far, the target imaging is too small, making it difficult to distinguish the details of the target effectively. Thus, the observation efficiency of this observation point is also scored as zero. Considering 10 times the optimal observation distance as the farthest cutoff point, we can establish a relative distance evaluation model and obtain the evaluation score m_d:

$$m_d = \begin{cases} 0, & H < \dfrac{Lf}{l}, \\ \left(\dfrac{10Lf/l - H}{9Lf/l}\right)^2 \times 100, & \dfrac{Lf}{l} \le H \le \dfrac{10Lf}{l}, \\ 0, & H > \dfrac{10Lf}{l}. \end{cases} \tag{12}$$

3.2. Image Motion Evaluation Model. During the inspection process, there are usually relative motions between the inspection spacecraft and the target spacecraft. During the exposure process of the observation camera, there will inevitably be relative motion between the image and the photosensitive object, resulting in the displacement of the target image point on the camera image plane, which is called image motion. Image shifting can cause image blurring and reduce imaging quality.

It is assumed that the speed of the target spacecraft relative to the inspection spacecraft is v_r. The image motion speed v_m on the image plane during two shots is

$$\frac{v_m \Delta t}{v_r \Delta t} = \frac{f}{H}. \tag{13}$$

The image motion speed on the image plane is

$$v_m = \frac{f}{H} v_r. \tag{14}$$

The image motion distance during the exposure time δ is

$$\delta = \frac{v_r f}{H} \Delta t. \tag{15}$$

Although the same amount of image motion distance, the degree of blurriness displayed varies along with the size of the target on the image plane varying. The ratio of image motion to the size of the target on the image plane can be used to characterize the degrees of blurriness of the image, that is δ_m.

$$\delta_m = \frac{\delta}{l}. \tag{16}$$

Substituting equations (11) and (15) into equation (16), then

$$\delta_m = \frac{v_r}{L} \Delta t. \tag{17}$$

When the fuzzy indicator δ_m exceeds the maximum value $\delta_{m\,\max}$, the observation image is unclear and the observation efficiency is scored as zero. Establish an image motion evaluation model to evaluate scores m_{id}:

$$m_{id} = \begin{cases} \left(1 - \dfrac{\delta_m}{\delta_{m\,\max}}\right) \times 100, & 0 \le \delta_m \le \delta_{m\,\max}, \\ 0, & \delta_m > \delta_{m\,\max}. \end{cases} \tag{18}$$

3.3. Effective Observation Time Evaluation Mode. To obtain sufficient information about the target spacecraft, it is usually desirable to have a sufficiently long effective observation time for the target under the constraints. Assuming that the inspection spacecraft observes and takes photos of the target at equal time intervals, the effective observation time can be represented by the number of effective photos N obtained in the inspection task. However, the effective observation time has a marginal effect; i.e., when the effective time reaches certain degrees, the observation efficiency of the task will not increase obviously. We have established an effective observation time evaluation model and the evaluating scores m_t:

$$m_t = \frac{N}{N + 40} \times 100. \tag{19}$$

3.4. Target Observation Angle Evaluation Model. On the other hand, it should be noticed that the inspection spacecraft carry out observations in all directions of the target spacecraft as much as possible for more information. Considering the target spacecraft as the center, it is tangentially divided into several (such as 32) equal-angle fan-shaped areas along the circumference. The more areas covered by the inspection spacecraft for effective observation, the more effective the observation. At the same time, an observation uniformity index is defined to measure the difference in effective observation of targets by the inspection spacecraft in different observation areas. In each area, if the number of photos taken by the inspection spacecraft is equal, it

Table 1: Initial relative state of two spacecraft.

Relative states	x (m)	y (m)	z (m)	$\dot{x}$ (m/s)	$\dot{y}$ (m/s)	$\dot{z}$ (m/s)
Target spacecraft	0	0	0	0	0	0
Inspection spacecraft	15000	0	0	-8.2178	3.3941	0

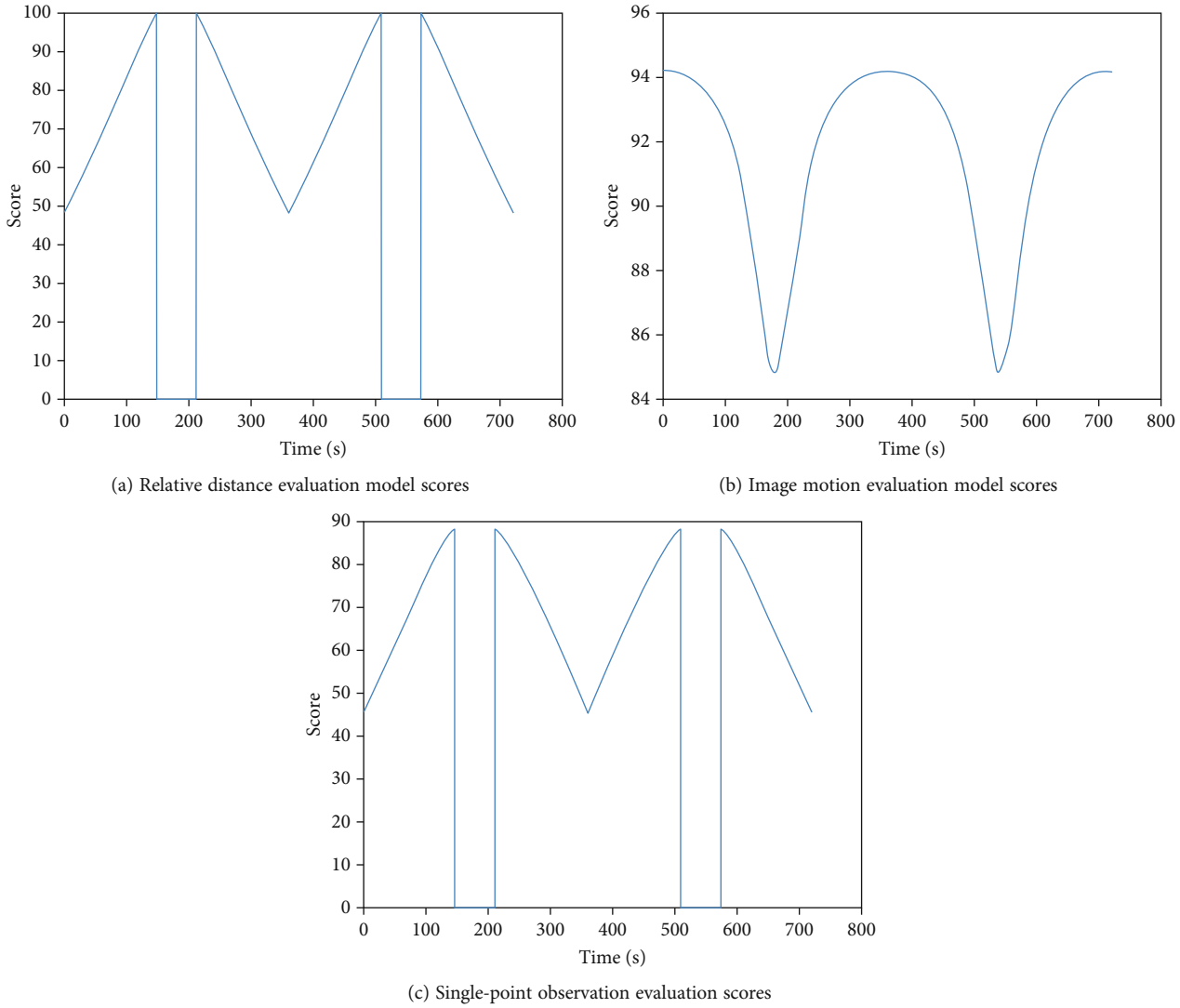

(a) Relative distance evaluation model scores

(b) Image motion evaluation model scores

(c) Single-point observation evaluation scores

Figure 4: Evaluation of single-point observation efficiency.

indicates that the observation is sufficiently uniform and the observation consistency at all angles of the target is the best.

$$f(\theta, \theta_i, s_\theta) = \begin{cases} 0, & |\theta - \theta_i| \geq s_\theta, \\ \dfrac{1}{s_\theta} - \dfrac{|\theta - \theta_i|}{s_\theta^2}, & \text{others}, \end{cases} \tag{20}$$

$$f_\theta(\theta) = \frac{1}{N}\sum_{i=1}^{N} f(\theta, \theta_i, s_\theta), \tag{21}$$

$$g_\theta(\theta) = \beta(\theta)\frac{1}{2\pi}, \tag{22}$$

$$\beta(\theta) = \begin{cases} 0.5, & \theta = \pm\pi, \\ 1, & \theta = \text{others}, \end{cases} \tag{23}$$

$$\Theta_k = -\pi + 2\pi\frac{k}{32}, 1 \leq k \leq 32, \quad s_\theta = \frac{2\pi}{32}. \tag{24}$$

θ_i is the angle of the inspection spacecraft relative to the

Table 2: Evaluation model scores for partial states and the whole task.

Experiment state	x (m)	y (m)	m_d	m_{id}	m_t	m_e	M
State 1	565	-268	87.9	91.8			
State 2	733	-233	80.5	92.8	98	63	74.5
State 3	899	-196	73.1	93.5			

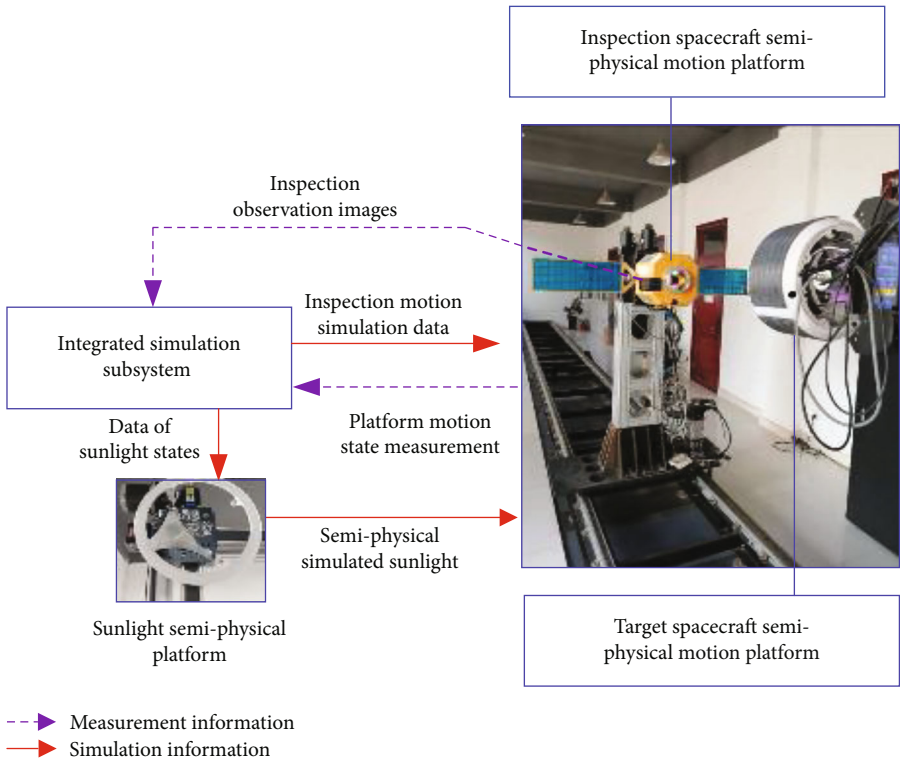

Figure 5: The semiphysical experiment system for close-range inspection.

target spacecraft when taking photo *No.i*. Therefore, the uniformity function of photo taking angle can be defined as

$$E_\theta = \sum_{k=0}^{32} \left(\frac{f_\theta(\Theta_k)}{g_\theta(\Theta_k)} - 1 \right)^2. \tag{25}$$

The more uniform the distribution of effective photos, the smaller the value E_θ. Establish a target observation angle evaluation model and evaluate scores m_e.

$$m_e = \frac{1}{1 + (1/3) \times \left(\left(E_\theta / \left(2.17 \times 10^3 \right) \right) - 1 \right)} \times 100. \tag{26}$$

3.5. Comprehensive Evaluation Model. Based on the models established above, the single-point observation efficiency evaluation model during the inspection process is m.

$$m_i = C \cdot m_d \cdot m_{id}, \tag{27}$$

where C is the constraint satisfaction coefficient. When C is 1, it means that the target meets all the observation constraints. Otherwise, if any of the observation constraint is not met, the C is 0.

In addition, taking account of the effective observation time evaluation and the target observation angle evaluation during the task process, the overall comprehensive effectiveness evaluation model of the inspection task is M.

$$M = \frac{m_t m_e}{N} \sum_{i=1}^{N} m_i. \tag{28}$$

m_i is the evaluation result of every single point during the inspection process, m_t is the evaluation result of the effective observation time of the task, and m_e is the evaluation result of the target observation angle of the task.

4. Theoretical Simulation Analysis

4.1. Example Configuration. Initially, the target spacecraft is set to be in a circular orbit at an altitude of 400 km above the ground, and the inspection spacecraft will fly around it. The inspection period is 720 s, and the camera takes photos every 5 seconds. The initial relative states of the two spacecraft

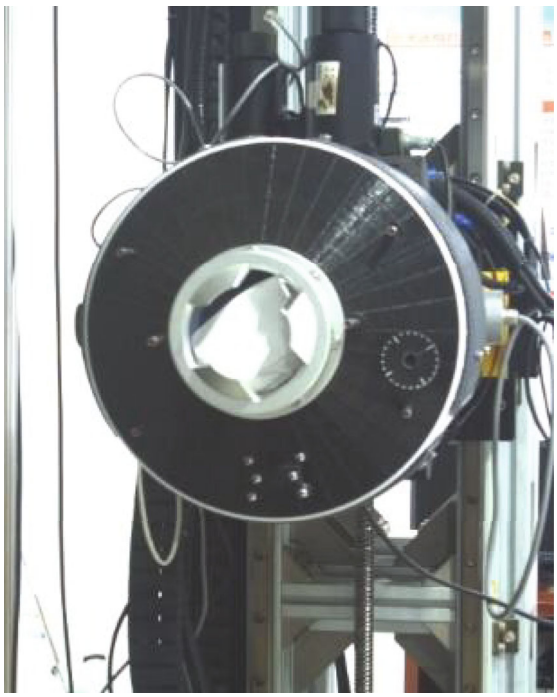

(a) State 1

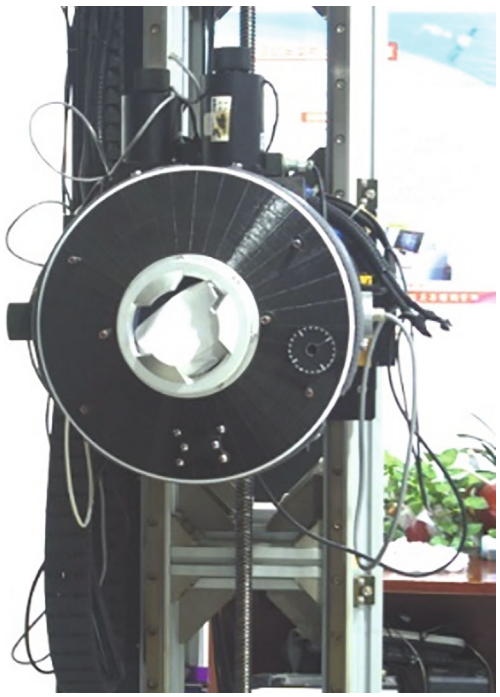

(b) State 2

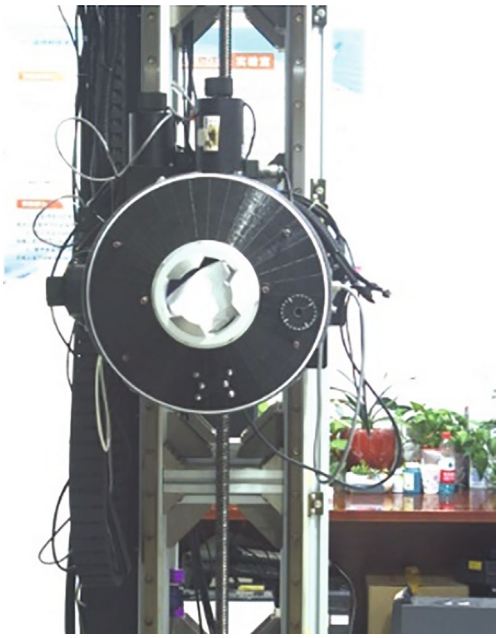

(c) State 3

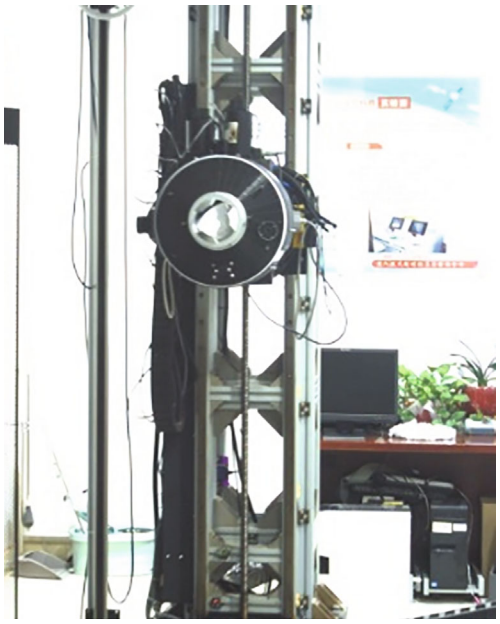

(d) State 4

Figure 6: Continued.

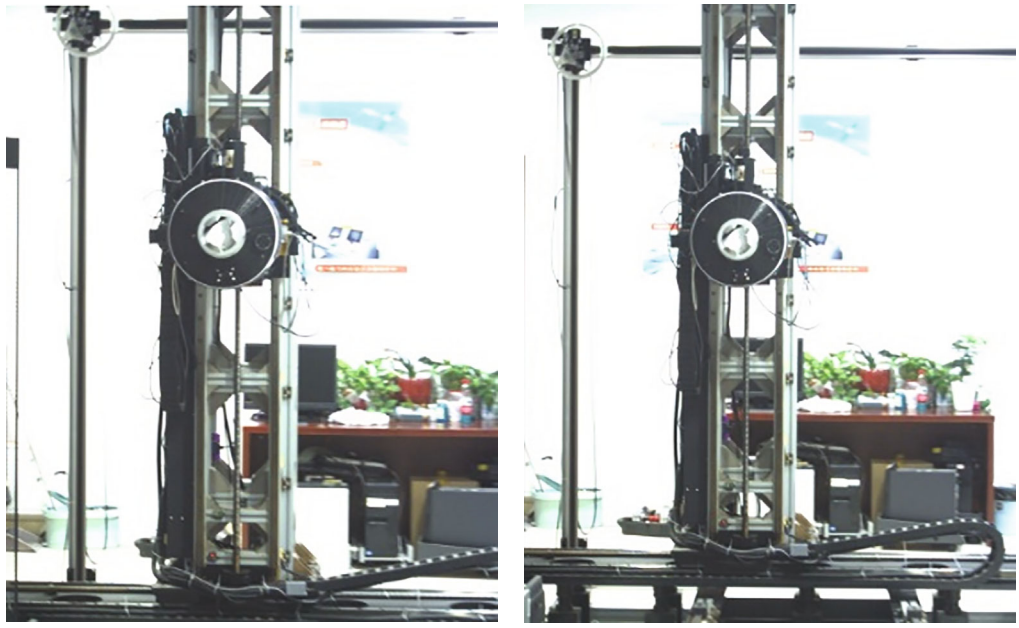

(e) State 5 (f) State 6

Figure 6: Photos of double ellipse flying inspection semiphysical experiment.

defined in the target orbit coordinate system are shown in Table 1.

4.2. Analysis of Simulation Results. According to equations (12) and (18), the performance scores of the relative distance evaluation model and the image motion evaluation model during the task process can be obtained, as shown in Figures 4(a) and 4(b). Figure 4(c) shows the variation of task observation effectiveness evaluation scores over time.

From Figure 4, it shows that the observation efficiency score of the relative distance evaluation model ranges from 50 to 100 points with a significant change, indicating that the relative distance has a significant impact on the quality of the observation graph. The score of the image motion evaluation model is between 85 and 95, indicating that the relative velocity effect is not significant, which is consistent with the lower relative velocity configured in the example. The comprehensive score of observation task effectiveness ranges from 45 to 85 points.

Furthermore, we select three states during the observation process for quantitative analysis, and the evaluation scores are shown in Table 2.

According to the above table, it shows that the average relative distance evaluation score m_d for each state is 80.5 points, and the average image motion evaluation score m_{id} is 92.7 points. It indicates that this task is less affected by relative distance and image motion factors. The model evaluation results are consistent with the parameter settings with a smaller relative distance and relative speed. The effective observation time evaluation score m_t for the current task is 98 points, indicating a longer observable time. The score of effective observation angle evaluation m_e is 63 points, mainly due to the influence of the target observation angle as there are some unobservable areas, which results in incomplete target observation. The overall effectiveness evaluation score M is 74.5 points, indicating that the whole effectiveness of the inspection task is common.

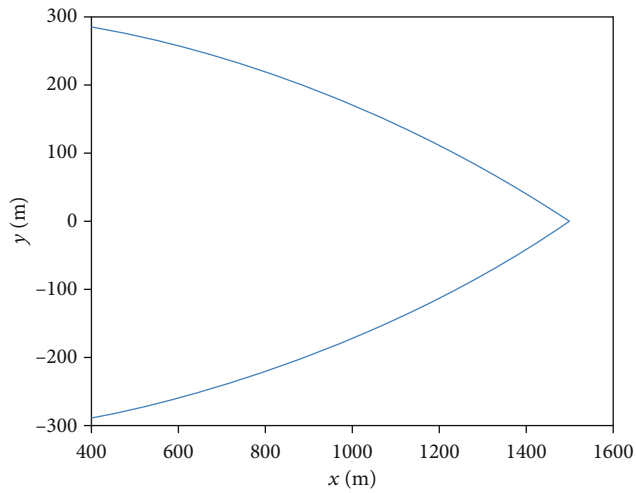

Figure 7: Double ellipse flying inspection experiment trajectory.

5. Semiphysical Experiment Validation

5.1. Semiphysical Experiment Environment. For further validation of the proposed evaluation models, a semiphysical close-range inspection experiment system is designed and carried out based on the 9-degree of freedom spatial relative motion simulation platform in our laboratory. The semiphysical experiment system has two semiphysical models of the inspection spacecraft and the target spacecraft, inspection observation cameras, an integrated simulation subsystem,

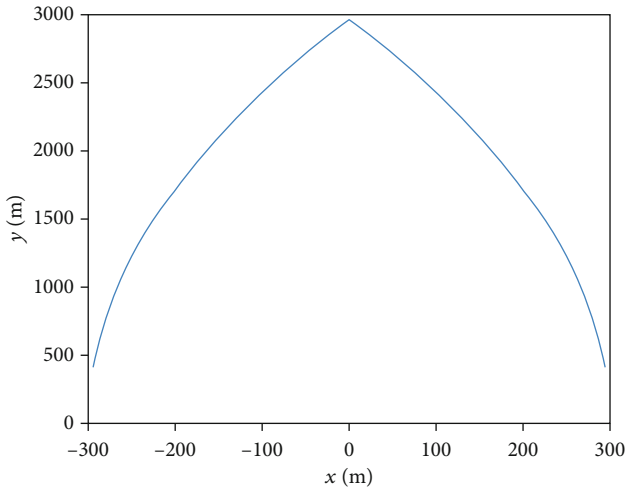

Figure 8: Double water-droplet flying inspection experiment trajectory.

and a semiphysical sunlight simulation platform, as shown in Figure 5.

The motion platform mainly consists of an inspection spacecraft motion platform and a target spacecraft motion platform which implement the semiphysical simulation of the relative motions with a 3-degree of freedom orbit during the inspection process and the respective 3 degrees of freedom attitude motion for each of the two spacecraft. The motion platform can carry out experiments with a position accuracy of 2 mm and an attitude accuracy of 0.05°. Two scaled spacecraft physical models as same as the inspection cameras are installed on the motion platform. Based on the inspection dynamic models, the integrated simulation subsystem solves the inspection motion and drives the motion platform to conduct a semiphysical simulation of the inspection motions. The integrated simulation subsystem simultaneously generates sunlight status data during the inspection process and drives the sunlight simulation platform to complete the simulation of the sunlight.

According to the common space optical cameras used both domestically and internationally, the inspection camera is selected to be equipped with CMOS sensors A5131CG75with a lens MH0820S whose pixel size is 2.4 μm. The camera's exposure time is variable from 1 μs to 1 s, and the field of view angle is 47.9°∗32.9°. The camera's distortion is less 0.1%, and the resolution ratio is 1280 ∗ 1024 pixels.

5.2. Experiment Design. The initial conditions of the semiphysical experiments are consistent with the theoretical simulation examples in Section 4.1. Two experiment conditions are designed, namely, double ellipse flying inspection and double water-droplet flying inspection. The experiments are repeated 10 times in each condition, and the results of 10 experiments are compared and analyzed with the results of the evaluation model. Due to the distance of the semiphysical motion platform being 12 m, we employ a scaled experiment method. The scaled rate of the motions is 400 : 1, and the scaled rate of the spacecraft physical models is 10 : 1; other scaled rates such as the velocity and acceleration are designed based on similarity criteria, as shown in Figure 6.

5.3. Analysis of the Experiment Results

5.3.1. Double Ellipse Flying Inspection Experiment. In the target orbit coordinate system, the initial position of the inspection spacecraft is [1500 m, 0,0], and the inspection period is 720 s. Then, we select a part of the trajectory from the inspection task for the semiphysical experiment, as shown in Figure 7.

Each experiment lasted for 264.5 seconds, and a total of 10 repeated experiments were conducted. Six separate statuses in the inspection process were selected randomly to take photos, as shown in Figure 6.

From the figure, it can be concluded that during the task process, the overall imaging of the target is clear. The practical imaging effect is consistent with the experiment conditions for low relative distance and low relative velocity, and the sun is not in the camera's field of view. Under this experiment condition, the inspection spacecraft can continuously obtain high-quality images of the target, which can complete the inspection task preferable.

5.3.2. Double Water-Droplet Flying Inspection Experiment. GSSAP conducts the inspections for noncooperative targets for identifying target types and work status, etc., usually within the inspection distance of about 10 km. However, for inspections such as in-orbit services, it is necessary to obtain the precise status of the target, and the inspection distance should be about 1 km. Double water-droplet trajectory would be better for such inspection tasks.

Setting the initial position of the inspection spacecraft to [300 m, 0,0] with the inspection period of 360 seconds, select a part of the trajectory from the inspection task for the semiphysical experiment, as shown in Figure 8.

Each experiment lasted for 155.5 seconds, and a total of 10 repeated experiments were conducted. Four separate statuses in the inspection process were selected randomly to take photos, as shown in Figure 9.

Figure 9 indicates that in these states, the target images are clear, which is more conducive to completing a fine inspection of the target. The experiment results meet the conditions of about 100 m inspection relative distance and also reflect the influence of experiment factors such as relative distance on the inspection observation results. Compared to state 1, state 4 has a relatively long distance and a smaller target, resulting in a decrease in observation imaging quality.

5.3.3. Summary of the Experiment Results. Comparing and analyzing the semiphysical experiment results with relevant research such as reference [14] for further validation, we select the results of 10 states randomly from two types of inspection experiments and summarize them in Table 3.

The results in the table show that the relative distance and image motion evaluation scores of each state extracted from the double elliptical orbit experiment are relatively high, with an average score of 81.6 points (it means that we can clearly identify the target's main features), indicating that the observation conditions of the relevant states are

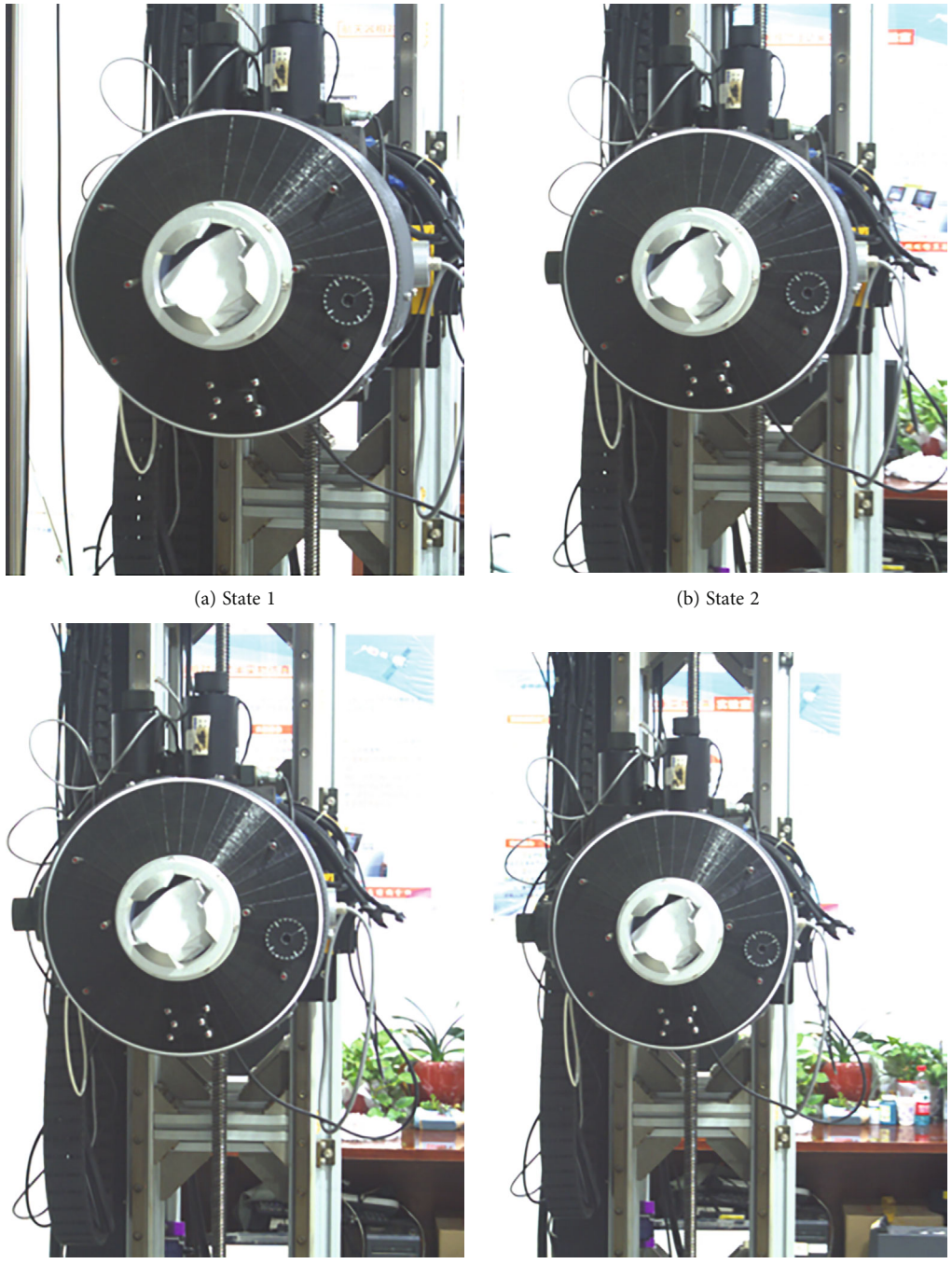

(a) State 1 (b) State 2

(c) State 3 (d) State 4

Figure 9: Photos of double water-droplet flying semiphysical experiment.

good. The practical semiphysical experiment images are consistent with the efficiency evaluation score based on the models. However, the effective observation angle for the target is only about 107°, which makes it impossible to obtain a comprehensive image of the target. The observation angle evaluation score is only 34 points, resulting in a comprehensive task evaluation score of 74.5 which means a common inspection efficiency.

The variations of the practical inspection photo in the double water-droplet flying experiment are also consistent with the variations of the evaluation scores from the effectiveness evaluation models. The average relative distance and image motion evaluation score is 87 points, indicating that the observation image quality is higher under observable conditions, but the effective observation angle for the target is only about 75°, the observation angle evaluation score is only 27 points, and the task evaluation score is 70.2 points.

The semiphysical experiment and evaluation model results show that the two typical close-range inspection trajectories' comprehensive efficiency of the inspection task is equivalent. The double ellipse flying inspection has a larger

Table 3: Summary of semiphysical experiments and evaluation results.

Semiphysical experiment		x (m)	y (m)	z (m)	m_d	m_{id}	m_t	m_e	M
Double ellipse flying experiment	State 1	565	-268	0	87.9	91.8	98	34	74.5
	State 2	733	-233	0	80.5	92.8			
	State 3	899	-196	0	73.1	93.5			
	State 4	1066	-152	0	65.9	93.9			
	State 5	1232	-100	0	58.9	94.1			
	State 6	1397	-41	0	52.1	94.2			
Double water-droplet flying experiment	State 1	-133	-599	0	88.5	95.8	97	27	70.2
	State 2	-108	-698	0	83.7	96.0			
	State 3	-80	-796	0	79.0	96.1			
	State 4	-43	-905	0	74.5	96.2			

observation angle for the target, but with a slightly poorer imaging quality, making it more suitable for comprehensive inspection of the target. The imaging quality of double water-droplet flying inspection is higher, but the observation angle of the target is smaller, making it more suitable for local fine inspection of the target.

Furthermore, we conducted a comparative simulation analysis of scheme optimization based on the evaluation results, taking circular inspection trajectory as an example. The simulation results show that the average comprehensive efficiency score of the optimized flight around inspection task is about 80 points, which is about 10% higher than before optimization.

6. Conclusion

This paper investigated an effectiveness evaluation method for space close-range inspection, which considers the sunlight constraint and other constraints. Then, the proposed evaluation model is validated through numerical simulations and semiphysical experiments. The following conclusions could be obtained:

(1) The developed comprehensive evaluation model is based on the factors such as the relative distance, the image shift, the effective observation time, and the target observation angle throughout the entire task process. Besides, the model covers the discrete states' evaluations and the process evaluation of space inspection tasks. So, the evaluation results are more effective and accurate

(2) The effectiveness of the developed model was validated through numerical simulations and 20 times semiphysical experiments. Besides, the comparison with previous literature research results validated the effectiveness of the evaluation models on the other hand

(3) In the two typical close-range inspection trajectories, the comprehensive efficiency of the inspection task is equivalent. However, the double elliptical flying inspection is more suitable for a comprehensive inspection of the target, and the double water-droplet flying inspection is more suitable for the local fine inspection of the target

The study has solved the problem of not considering the overall evaluation requirements along the task process, compared with the previous space inspection evaluation studies. And it expands the research and application further for the complete process of inspection tasks, which can better support the in-depth researches such as inspection strategy design and inspection trajectory optimization based on evaluation results.

Data Availability

Data is available on request (zhoujianyong@nudt.edu.cn).

Conflicts of Interest

The authors declare that they have no conflicts of interest.

References

[1] H. Weiss, A. Patel, M. Romano et al., "Methods for evaluation of human-in-the-loop inspection of a space station mockup using a quadcopter," in *2022 IEEE Aerospace Conference (AERO)*, Big Sky, MT, USA, March 2022.

[2] J. Boskovic, J. A. Jackson, and R. Wise, "Implementation & flight testing of the IMPACT system for autonomous ISR," in *AIAA Information Systems-AIAA Infotech @ Aerospace*, Grapevine, Texas, January 2017.

[3] S. Meister, L. Grundhöfer, J. Stüve, and R. M. Groves, "Imaging sensor data modelling and evaluation based on optical composite characteristics," *The International Journal of Advanced Manufacturing Technology*, vol. 116, no. 11-12, pp. 3965–3990, 2021.

[4] D. Neta and D. Vallado, "On satellite umbra/penumbra entry and exit positions," *The Journal of the Astronautical Sciences*, vol. 46, no. 1, pp. 91–103, 1998.

[5] H. R. Sheikh, A. C. Bovik, and G. de Veciana, "An information fidelity criterion for image quality assessment using natural scene statistics," *IEEE Transactions on Image Processing*, vol. 14, no. 12, pp. 2117–2128, 2005.

[6] C. Yang, B. Yu-zhu, and Z. Yong, "Modeling and simulation of optical observation for GEO belt," *Computer Simulation*, vol. 38, no. 1, pp. 10–13, 2021.

[7] J.-l. Wang, R. Wang, Z. Lu-wei et al., "On-orbit application research and imaging simulation analysis of GSSAP satellite," *Infrared and Laser Engineering*, vol. 52, no. 4, pp. 1–9, 2023.

[8] S. Zhao, N. Ruan, and X. Zhuang, "Detection ability of space-based optical observation system to space debris," in *Proceedings Volume 9678, AOPC 2015: Telescope and Space Optical Instrumentation*, pp. 112–119, Beijing, China, October 2015.

[9] M. Wang, C. Fan, J. Pan, S. Jin, and X. Chang, "Image jitter detection and compensation using a high-frequency angular displacement method for Yaogan-26 remote sensing satellite," *ISPRS Journal of Photogrammetry and Remote Sensing*, vol. 130, pp. 32–43, 2017.

[10] Z. Ying, N. Yan-xiong, Y. Lu et al., "Analysis and study on detection capability of satellite photoelectric imaging system," *Acta Optica Sinica*, vol. 34, no. 1, pp. 109–114, 2014.

[11] L. Lin-ling, *Research on Remote Sensing Image Quality Evaluation Method Combining Subjective and Objective Methods*, Nanjing University of Science and Technology, Nanjing, 2013.

[12] M. Lu, *Research on Remote Image Quality Assessment*, Harbin Institute of Technology, Harbin, 2013.

[13] D.-j. Wang, G.-q. Wu, H. Lu, J. Yao-xiang, L. Chong-hua, and S. Xiao-yu, "Analysis and research on GSSAP observation," *Aerospace Control and Application*, vol. 48, no. 3, pp. 22–28, 2022.

[14] Z. P. Hou, *Evaluation of Close-Range Optical Inspection Mission in Space and Hardware-in-the-Loop Simulation System*, National University of Defense Technology, Changsha, 2022.